THE JOURNAL OF PHYSICAL CHEMISTRY B

pubs.acs.org/JPCB Article

Pressure Induced Wetting and Dewetting of the Nonpolar Pocket of Deep-Cavity Cavitands in Water

Published as part of The Journal of Physical Chemistry virtual special issue "Peter J. Rossky Festschrift".

Du Tang, Tobias Dwyer, Hussain Bukannan, Odella Blackmon, Courtney Delpo, J. Wesley Barnett, Bruce C. Gibb, and Henry S. Ashbaugh*

Cite This: https://dx.doi.org/10.1021/acs.jpcb.0c02568

ABSTRACT: Hydrophobic interactions drive the binding of nonpolar ligands to the oily pockets of proteins and supramolecular species in aqueous solution. As such, the wetting of host pockets is expected to play a critical role in determining the thermodynamics of guest binding. Here we use molecular simulations to examine the impact of pressure on the wetting and dewetting of the nonpolar pockets of a series of deep-cavity cavitands in water. The portals to the cavitand pockets are functionalized with both nonpolar (methyl) and polar (hydroxyl) groups oriented pointing either upward or inward toward the pocket. We find wetting of the pocket is favored by the hydroxyl groups and dewetting is favored by the methyl groups. The distribution of waters in the pocket is found to exhibit a two-state-like equilibrium between wet and dry states with a free energy barrier between the two states. Moreover, we demonstrate that the pocket hydration of the cavitands can be collapsed onto a unified adsorption isotherm by assuming the effective pressures within each cavitand pocket differ by a shift pressure that depends on the chemical identity and number of functional groups placed about the portal. These observations support the development of a two-state capillary evaporation model that accurately describes the equilibrium between states and naturally gives rise to the effective shift pressures observed from simulation. This work demonstrates that the hydration of host pockets can be tuned following simple design rules that in turn are expected to impact the thermodynamics of guest complexation.

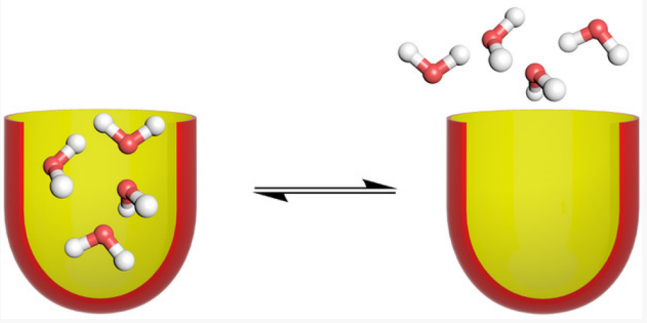

INTRODUCTION

Near water vapor/liquid coexistence, idealized, purely repulsive hydrophobic surfaces in aqueous solution are predicted to be enshrouded within a vapor-like layer as a result of the preferential self-hydration of water over interfacial wetting.[1−6] Confining water between nonpolar mesoscale surfaces or within nonpolar pockets is subsequently predicted to nucleate solvent evaporation, magnifying attractive hydrophobic interactions between nonpolar moieties.[2,7−11] This nebulous vapor layer, however, is suppressed by ubiquitous van der Waals interactions that draw liquid water back into contact with the solute surface.[12] Nevertheless, water density fluctuations next to realistic, extended hydrophobic surfaces have been shown to be akin to those at a vapor/liquid interface,[13] indicating the neighboring solvent density alone is insufficient for quantifying the hydrophobicity of mesoscale and larger interfaces.[14]

The potential relevance of hydrophobic dewetting phenomena is highlighted by experimental and theoretical results indicating that the nonpolar cavities of some proteins spontaneously dry in water to impact their function. For instance, crystallographic and molecular simulation studies of the L99A mutant of T4 lysozyme provided some of the first evidence of a drying transition within a protein's nonpolar cavity.[15] While dry at atmospheric pressure, water was shown to cooperatively fill lysozyme's internal nonpolar cavity with increasing pressure (∼1000 bar), providing a mechanism for protein denaturation. Alternately, the conduction of sodium across pentameric ligand-gated ion channels is regulated by subtle iris-like conformational changes about the transmembrane pore.[16] In the open state, the pore is fully hydrated, but in the closed state, hydrophobic isoleucine residues constrict the aperture and induce drying of a 15 Å long segment of the channel. This blocks free ion passage despite the fact the pore is still large enough to permit solvent

Received: March 23, 2020
Revised: May 11, 2020
Published: May 13, 2020

egression. Similar vapor-lock gating mechanisms have been proposed for the nicotinic acetylcholine receptor[17] and *Escherichia coli*'s small mechanosensitive channel.[18] Finally, NMR and molecular dynamics simulation studies have found that the ligand-binding pocket of bovine β-lactoglobulin is largely devoid of water under ambient conditions, with only fleeting filling events.[19] Dewetting of this hydrophobic pocket is thereby expected to impact the kinetics and thermodynamics of fatty acid binding to this apoprotein.

Considering the wetting of a model hemispherical nonpolar pocket in water, Setny et al.[20] demonstrate that the stability of water in the pocket is dependent on the approach of nonpolar ligands. When the ligand was far away, water was found to freely fluctuate between all possible hydration states from zero (dry) to 10 (wet) waters within the pocket with practically no free energy differences between states. As the ligand approached the pocket opening, the hydration free energy landscape was found to dramatically change to a bimodal distribution between wet and dry states with a barrier between them. Upon ligand binding, the dry state becomes dominant. This drying-mediated ligand binding in this model system was shown to be dominated by a favorable enthalpy of association resulting from gaining water−water attractive interaction upon release from the pocket and opposed by an unfavorable entropy of association.[21,22] This observation stands in opposition to traditional descriptions of hydrophobic interactions, which associate nonpolar solute aggregation with a strongly favorable entropy resulting from the release of structured waters from nonpolar surfaces.[23] Indeed, enthalpically driven association has been experimentally observed for guests binding to proteins and supramolecular species in water.[24,25] Nau and co-workers[26,27] have interpreted this "non-classical hydrophobic interaction" in terms of high-energy waters that forfeit hydrogen bonds within nonpolar pockets. They have demonstrated a strong correlation between lost hydrogen bonds and the binding constants between a range of supramolecular hosts and nonpolar guests. This correlation, however, does not account for the equilibrium between wet and dry states observed by Setny et al.[20] and theoretically predicted for water under nonpolar confinement.

Deep-cavity cavitands are a class of water-soluble, bowl-shaped supramolecular host species possessing a nonpolar guest binding pocket that is approximately 8 Å deep with a portal opening approximately 8 Å wide (Figure 1).[28,29] These concave hosts resemble the model hydrophobic pockets

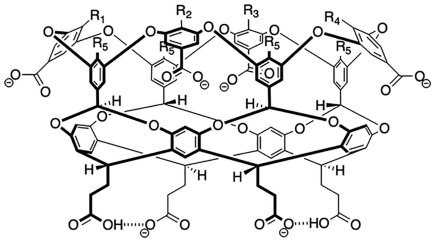

octa-acid (OA): $R_1 - R_5 = H$
mono-*endo*-methyl octa-acid (MEMOA): $R_1 = CH_3$, $R_2 - R_5 = H$
1,3-di-*endo*-methyl octa-acid (DEMOA): $R_1 = R_4 = CH_3$, $R_2 = R_3 = R_5 = H$
tri-*endo*-methyl octa-acid (TrEMOA): $R_1 - R_3 = CH_3$, $R_4 - R_5 = H$
tetra-*endo*-methyl octa-acid (TEMOA): $R_1 - R_4 = CH_3$, $R_5 = H$
tetra-*exo*-methyl octa-acid (TEXMOA): $R_1 - R_4 = H$, $R_5 = CH_3$
tetra-*endo*-hydroxyl octa-acid (TEMOA): $R_1 - R_4 = OH$, $R_5 = H$
tetra-*exo*-hydroxyl octa-acid (TEXHOA): $R_1 - R_4 = H$, $R_5 = OH$

Figure 1. Chemical structures of the eight deep-cavity cavitands simulated here.

considered by Setny and co-workers.[20−22] Appropriately sized nonpolar and amphipathic guests readily bind to the cavitand pocket facilitated by hydrophobic interactions. As such, understanding the hydration of the cavitand pocket is expected to help elucidate the role of the solvent in driving guest recognition and binding.[30] Recently, we demonstrated through a combination of both experiment and simulation that the hydration of the nonpolar pocket of cavitands depends sensitively on the functionalization of the host portal.[31] In particular, it was established that, while water wets the pocket of the nonfunctionalized parent cavitand octa-acid (OA, Figures 1 and 2), the pocket of tetra-*endo*-methyl octa-acid

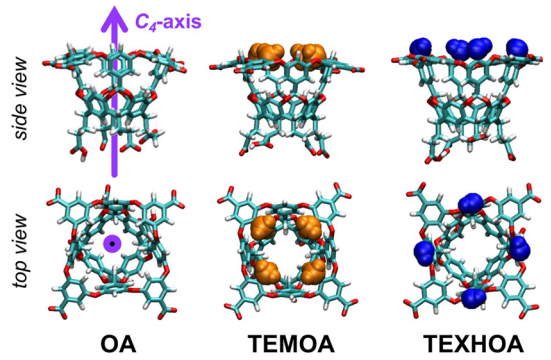

Figure 2. Molecular snapshots of the parent cavitand, octa-acid (OA), and an *endo*-functionalized, tetra-*endo*-methyl octa-acid, and *exo*-functionalized cavitand (TEMOA), tetra-*exo*-hydroxyl octa acid (TEHOA), host. The body of the parent cavitand is illustrated in licorice format, while the functional groups are illustrated using a van der Waals representation. The cavitands are shown from the side showing the height of the walls of the pocket from the top and looking down into the pocket through the portal. The 4-fold C_4-axis of rotational symmetry is denoted by the purple arrow pointing through the side view and up from the pocket of OA.

(TEMOA, Figures 1 and 2), differing from OA by four methyl groups oriented inward toward the pocket, is dry a significant fraction of the time. Dewetting of the pocket was found to be consistent with thermodynamic equilibrium between liquid and vapor states driven by interfacial forces. The drying of TEMOA was manifested in stronger binding of sodium alkyloate guests compared to OA, favored by a dominant enthalpy and opposed by a weaker entropy, illustrative of the "non-classical hydrophobic interaction". This work illustrated that hydration of host pockets is a potential synthetic design target for tailoring guest binding, subject to subtle changes in the environment ringing the binding site.

Seeking to expand our prior work, we report here a molecular dynamics simulation study of the impact of the functionalization of deep-cavity cavitands on the hydration of their nonpolar binding pockets. In addition to the parent, nonfunctionalized, cavitand octa-acid (OA), we consider seven additional cavitands with varying functionalities (Figure 1): mono-*endo*-methyl octa-acid (MEMOA), 1,3-di-*endo*-methyl octa-acid (DEMOA), tri-*endo*-methyl octa-acid (TrEMOA), tetra-*endo*-methyl octa-acid (TEMOA), tetra-*exo*-methyl octa-acid (TEXMOA), tetra-*endo*-hydroxyl octa-acid (TEHOA), and tetra-*exo*-hydroxyl octa-acid (TEXHOA). The portals of the functionalized cavitands are ringed by either nonpolar (methyl) or polar (hydroxyl) groups that are oriented at either inward pointing *endo* positions or upward pointing *exo* positions relative to the host pocket (Figures 1 and 2). In

https://dx.doi.org/10.1021/acs.jpcb.0c02568
J. Phys. Chem. B XXXX, XXX, XXX−XXX

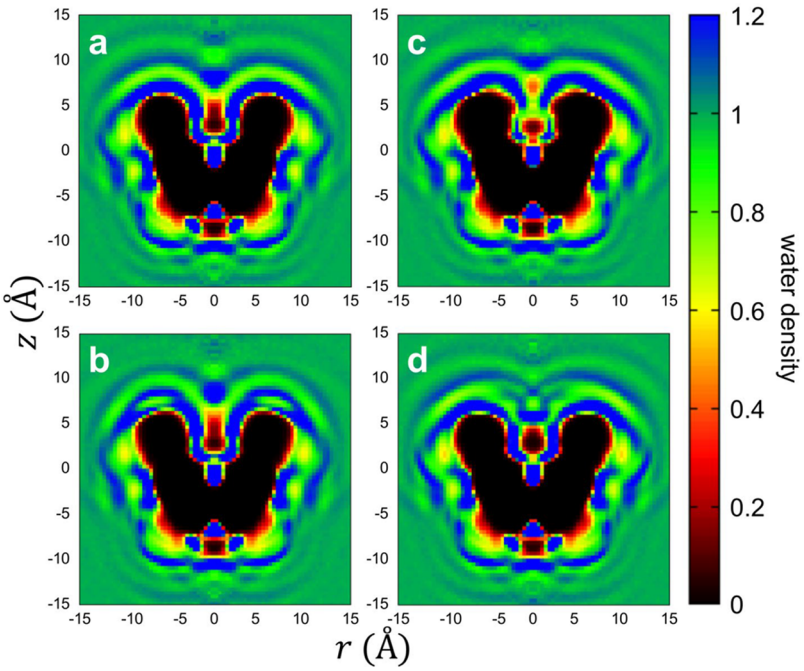

Figure 3. Average water density distribution about the hosts OA (a), TEXMOA (b), TEMOA (c), and TEHOA (d). The water density is cylindrically averaged about the C_4-axis of symmetry for each of the hosts, with r corresponding to the radial distance from the C_4-axis and z indicating the vertical rise relative to the cavitand center-of-mass. The densities follow the color key on the right-hand side of the figure.

addition, the series OA, MEMOA, DEMOA, TrEMOA, and TEMOA examines the impact of increasing the hydrophobicity of the portal. While the hosts MEMOA, DEMOA, TrEMOA, TEHOA, and TEXHOA have not been synthesized to date, they can be examined using simulations to gain valuable insights into pocket hydration. We analyze pocket hydration in terms of the spatial distribution of waters about the entire host, pocket hydration probability distributions, and the mean water adsorption within the pocket. The thermodynamics of water adsorption are subsequently quantified within the context of a hydration distribution model. Finally, we construct a two-state capillary evaporation model to gain insight into the forces governing the extent of pocket hydration and the role of the functional groups ringing the portal.

METHODS

Molecular dynamics simulations of a range of functionalized cavitands in water were performed using GROMACS 5.1.[32] Simulations were performed in the isothermal−isobarric ensemble at 25 °C with pressures ranging from −1000 to 2500 bar (−750, −500, −250, 1, 500, 1000, 1500, 2000, and 2500 bar). The temperature and pressure were controlled using a Nosé−Hoover thermostat[33] and Parrinello−Rahman barostat,[34] respectively. Water was modeled using the TIP4P/EW potential.[35] The cavitands and their counterions were modeled using the generalized Amber force Field.[36] The charge of each cavitand was set to be −6e to match the protonation state at pH 7.[30] The four benzoic acid groups around the rim of the cavitand and two of the four benzoic acid groups on the feet were deprotonated (Figure 1). The partial charges of each atom were obtained by AM1-BCC calculations following geometry optimization.[37] Different from our previous work which considered scaled charges in its modeling of cavitands,[31] here we assume the cavitands adopt their full charge. This tilts hydration of the host pockets toward wet states but does not impact the underlying physics of cavitand wetting/dewetting. Eight distinct cavitands with varying functional groups added about the portal to the hydrophobic pocket were simulated (Figure 1): octa-acid (OA), mono-*endo*-methyl-octa-acid (MEMOA), 1,3-di-*endo*-methyl-octa-acid (DEMOA), and tri-*endo*-methyl-octa-acid (TrEMOA), tetra-*endo*-methyl-octa-acid (TEMOA), tetra-*exo*-methyl-octa-acid (TEXMOA), tetra-*endo*-hydroxyl-octa-acid (TEHOA), and tetra-*exo*-hydroxyl-octa-acid (TEXHOA). These cavitands exhibit varying degrees of methylation, hydroxylation, and orientations of functional groups about the pocket portal. Nonbonded Lennard-Jones interactions were truncated beyond a separation of 9 Å with a mean-field dispersion correction for longer-range contributions to the energy and pressure. Cross Lennard-Jones interactions between unlike species were determined using Lorentz−Berthelot combining rules.[38] Particle mesh Ewald summation with a real space cutoff of 9 Å was applied to calculate electrostatic interactions.[39] Bond lengths involving hydrogens for the cavitands were held fixed using the LINCS algorithm,[40] while water was held rigid using SETTLE.[41] In each simulation, a single cavitand was solvated in 2000 water molecules. Production runs were conducted for 200 ns following an equilibration run of 5 ns. The equations of motion were integrated using a 2 fs time step. Configurations were saved every 1 ps for postsimulation analysis of thermodynamic averages.

Water densities about the cavitands were determined by assuming the hosts are effectively symmetric about their C_4-axis (Figure 2). This approximation allows us to adopt a cylindrical coordinate system to bin water densities about the cavitand and characterize the mean pocket hydration state.

The number of waters within a cavitand pocket, n, was determined by constructing a hexahedron bounding the pocket and counting the number of waters within the polyhedron. The top face of the hexahedron was determined by constructing a

https://dx.doi.org/10.1021/acs.jpcb.0c02568
J. Phys. Chem. B XXXX, XXX, XXX−XXX

plane fitted through the eight diphenyl ether oxygen atoms ringing the pocket portal, while the bottom face was determined by the four carbon atoms to which the acid feet are attached to the bottom of the pocket. The remaining four faces were determined by planes passing through oxygen atoms at the portal and carbon atoms at the bottom following the 4-fold rotational symmetry of the cavitand (Figure 2). Hydration state probability distribution functions were determined from analysis of the number of waters in the pocket over saved configurations.

Finally, we considered the impact of the number of waters within a host pocket on its partial molar volume. The partial molar volume of OA as a function of the pocket hydration state was determined by taking the difference in the average simulation volume of the cavitand with n waters in the pocket less the average volume of a simulation box of pure water with the same number of waters as in the cavitand mixture

$$v(n) = \langle V(n)\rangle_{c+w} - \langle V\rangle_{w} \quad (1)$$

where the angled brackets ($\langle ... \rangle$) indicate simulation averages of the system volume determined with (c + w) and without (w) the cavitand, while the argument n indicates the number of waters in the host pocket.

RESULTS AND DISCUSSION

Cavitand Pocket Hydration. The average water density about OA, TEXMOA, TEMOA, and TEHOA is illustrated in Figure 3. The density in these plots is cylindrically averaged about the host C_4-axis of symmetry to clearly visualize the water distribution. The cavitands sit in the U-shaped black outline in these plots, corresponding to the location of the heavy atoms of the host where the water density is zero. Water readily packs about the outside of the cavitands, as indicated by the high-density regions ($\rho > 1.2$ g/cm^3, denoted in blue) from the rim of the pocket to the foot of the cavitand, forming approximately three water shells. In the case of OA (Figure 3a), water readily enters the hydrophobic pocket and packs against the inner walls of the host; however, there is a region of depleted water density along the centerline of the cavitand within the pocket where the density drops to zero. This depletion is attributable to the van der Waals attractions between the waters and cavitand drawing the solvent to the inner walls of the host. One of the most significant adsorption regions for water is the bottom of the pocket, where a large increase in water density is observed. This adsorption site is big enough for a single water, which enjoys hydrogen-bonding with the four inner pointing hydrogens at the bottom of the pocket (Figures 1 and 2). The distribution of water about TEXMOA (Figure 3b) closely follows that of OA, with only a slight depletion of waters near the rim of the pocket due to the presence of the four *exo*-pointing methyl groups at the top of the cavitand. More significant perturbations in the water density are observed for TEMOA (Figure 3c). While the packing of water on the exterior of TEMOA is comparable to that for OA and TEXMOA, the water density along the inner walls of TEMOA's pocket is reduced. We do observe, however, a slight increase in the water density at the top of the pocket, which we believe can be attributed to favorable attractive interactions between water and the four *endo*-pointing methyls. For TEHOA, we find water rewets the cavitand pocket, as indicated by the increase in water density along the inner walls of this host (Figure 3d), comparable to the wetting of OA and TEXMOA. An additional increase in water density is observed at the top of TEHOA's pocket ($z \approx 5$ Å) supported by hydrogen-bonding between the *endo* hydroxyl groups and water that makes pocket hydration favorable. We conclude from the analysis of water's density that, while the distributions of water outside of all of the cavitands are effectively the same, the hydration of the hydrophobic pocket depends sensitively on the rim functionalization.

The hydration of the host pocket is dynamic, with the number of waters within the cavitand continuously fluctuating. To capture the fluctuating nature of the pocket hydration, it is more informative to consider the probability distribution of hydration states. Figure 4 shows the hydration number

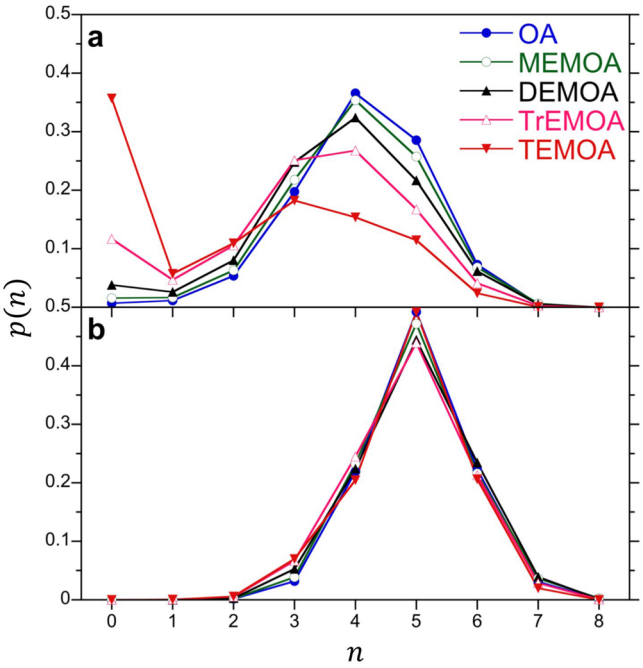

Figure 4. Hydration number probability distributions for water in the pockets of OA and *endo*-methyl functionalized hosts (MEMOA, DEMOA, TrEMOA, and TEMOA) at 25° and pressures of 1 bar (a) and 2500 bar (b). The figure symbols are defined in the legend. Error bars are comparable in size or smaller than the symbols.

probability distribution for water in OA, MEMOA, DEMOA, TrEMOA, and TEMOA at 1 and 2500 bar, illustrating the impact of increasing the hydrophobicity of the pocket portal. At atmospheric pressure, OA exhibits a unimodal probability distribution (Figure 4a), with 4 waters being the most probable hydration state. This distribution is not symmetric, as would be expected for a normal distribution, but is skewed slightly toward lower occupancy states. As such, while the probability of observing 8 (= 4 + 4) waters in OA's pocket is effectively zero, the probability of observing an empty pocket (0 = 4 − 4) is finite. This asymmetry is accentuated as the portal methylation increases. While we never observe more than 8 waters in the pocket, the probability of observing an empty pocket systematically increases from 1% for OA to 36% for TEMOA. Moreover, increasing portal methylation changes the distribution from unimodal for OA and MEMOA to bimodal for DEMOA, TrEMOA, and TEMOA. The second peak of the bimodal distributions occurs for the empty pocket, with a minimum between the two peaks occurring at $n = 1$. The position of the primary peak shifts from 4 waters for OA through TrEMOA to 3 waters for TEMOA. While not a true

https://dx.doi.org/10.1021/acs.jpcb.0c02568
J. Phys. Chem. B XXXX, XXX, XXX−XXX

phase equilibrium between a liquid and vapor, the rise of the second, low-density state with increasing *endo*-methylation is reminiscent of capillary evaporation driven by decreasing pore wettability (*vide infra*). While not shown here, the hydration distribution for water in TEXMOA is practically indistinguishable from that of OA. This suggests that pointing the methyl groups away from the pocket limits their influence on pocket hydration.

It may be thought that the increasing methylation may impact the shape of the pocket, thereby playing a role in the hydration state distributions observed at atmospheric pressure. If we increase the pressure to 2500 bar, the dry ($n = 0$) state is suppressed and the distributions are unimodal (Figure 4b). The most probable pocket hydration state at elevated pressure is 5 waters as a result of pressure pushing more waters into the pocket. While there are subtle differences between the hydration distributions for all of the cavitands, the shapes of the distributions are practically the same. This suggests no significant role for portal functionalization on the shape and volume of the pocket available for water adsorption.

Different from methylation, adding polar hydroxyl groups about the portal can drive the host pocket to be more favorably wetted. The impact of functionalizing the portal with hydroxyl groups placed at the *exo*- and *endo*-positions at atmospheric pressure is shown in Figure 5. While the methyl groups play

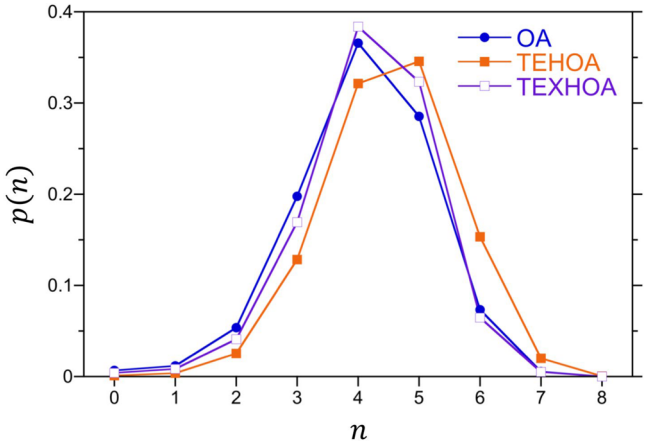

Figure 5. Hydration number probability distributions for water in the pockets of OA and the hydroxyl functionalized hosts (TEHOA and TEXHOA) at 25 °C and 1 bar. The figure symbols are defined in the legend. Error bars are comparable in size or smaller than the symbols.

almost no role in the hydration of TEXMOA, for TEXHOA, we find the larger occupancy states are preferentially stabilized compared to the OA. As such, the $n = 4$ and 5 occupancy states are slightly more probable for TEXHOA than OA. For TEHOA, the shift to higher pocket occupancy states is even more profound with $n = 5$ becoming the more probable hydration state, with the distribution becoming more symmetric.

The pocket hydration state can be manipulated by changing the system pressure, as suggested in Figure 4. In Figure 6, we provide a more detailed account of the pressure dependence of the pocket hydration distribution for OA and TEMOA. While we only observed a unimodal hydration distribution for OA above, Figure 6a shows that a second maximum in the distribution can be obtained by dropping the pressure to negative values, placing the water under tension (metastable).

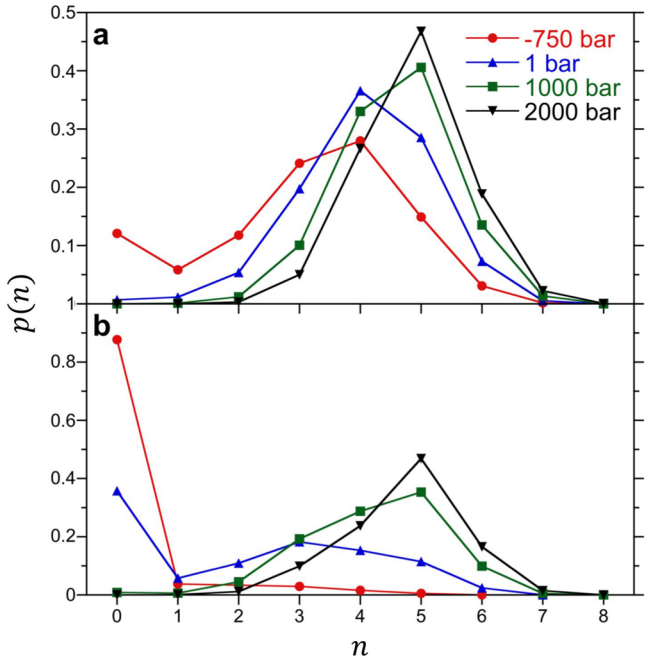

Figure 6. Impact of pressure on the hydration number probability distributions for water in the pockets of OA (a) and TEMOA (b) at 25 °C. The figure symbols are defined in the legend. Error bars are comparable in size or smaller than the symbols.

Specifically, as the pressure drops, the probability of observing OA to be empty increases from 1% at 1 bar to 12% at −750 bar. The first hint of a secondary maximum for the empty cavitand occurs at −500 bar (not shown), where the probability of observing an empty cavitand is more probable than observing a single water in the pocket (i.e., $p(0) > p(1)$). The empty cavitand is even more probable at −750 bar. Similar to the hydration distribution for TEMOA reported above (Figure 4a), OA under tension exhibits another maximum at $n = 4$ separated from the empty state by a minimum (free energy barrier) at $n = 1$. While the empty cavitand presumably could be further stabilized by dropping the pressure further, the simulations became too unstable and failed. The pressure induced stabilization of the empty cavitand is even more prominent for TEMOA (Figure 6b), which is empty ∼90% of the time at −750 bar. At this pressure, the hydration probability distribution for TEMOA is a monotonically decreasing function of the occupation state and a second maximum is not observed. Comparing OA and TEMOA, the hydration distributions for OA correspond roughly to those for TEMOA at a pressure 1000 bar greater. Overall, the pressure dependencies of the hydration distributions for OA and TEMOA are consistent with water exhibiting two-state-like equilibria between a dewetted/empty state and wetted/filled state.

Thermodynamics of Pocket Hydration. Rather than the individual hydration state probabilities, an alternate way of examining pocket hydration is to consider the average number of waters in a cavitand pocket as a function of pressure. The average number of waters in the pocket is determined by the sum

$$\langle n \rangle = \sum_{i=1}^{\infty} ip(i) \tag{2}$$

https://dx.doi.org/10.1021/acs.jpcb.0c02568
J. Phys. Chem. B XXXX, XXX, XXX−XXX

We compare $\langle n \rangle$ as a function of pressure for all of the simulated cavitands in Figure 7. Generally speaking, the mean

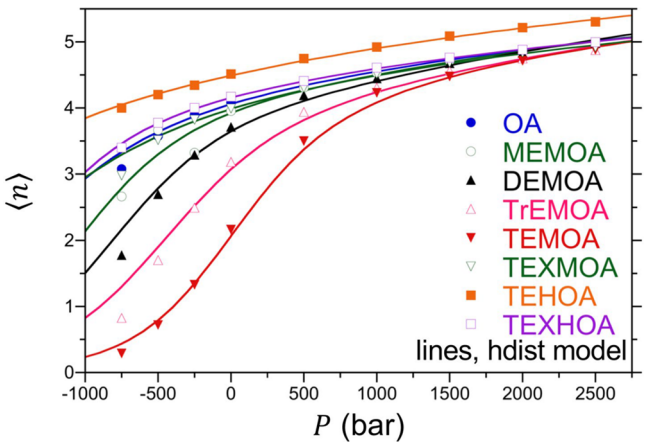

Figure 7. Mean pocket hydration numbers for all simulated cavitand hosts as a function of pressure at 25 °C as determined from simulation and fits to the hydration distribution model (hdist). The figure symbols are defined in the legend. Error bars are comparable in size or smaller than the symbols.

hydration number is an increasing function of pressure for all of the cavitands. The hydrophobic, *endo*-functionalized cavitands typically have lower occupation numbers than OA at constant pressure, with $\langle n \rangle$ systematically decreasing with increasing methylation. Conversely, TEHOA exhibits greater pocket hydration than OA over the entire pressure range. The impact of functionalization of the *exo*-position by either methyl or hydroxl groups, on the other hand, only exerts a minor perturbation on the pocket hydration relative to OA. For the most hydrophobic pockets (i.e., DEMOA, TrEMOA, and TEMOA), the water binding isotherm appears sigmoidal, indicating water adsorption is cooperative. As the pocket hydrophobicity decreases, however, the water binding isotherms systematically shift to lower pressures, obscuring the sigmoidal shape of the binding isotherms for the more hydrophilic cavitands (e.g., TEHOA). Taken together, these binding isotherms suggest water wets the pocket following two-state-like behavior, as suggested by the probability distributions described above.

We can construct an analytical expression for the adsorption isotherm of an individual cavitand by considering the pressure dependence of the pocket hydration free energies. Specifically, the relative hydration free energy of a host pocket with n waters in it is

$$\Delta G(n) = -kT \ln\left(\frac{p(n)}{p(4)}\right) \tag{3}$$

where we have chosen $n = 4$ as the reference state from which we measure the free energy. While the bulk water outside the cavitand is compressible, if we assume that the volume difference between discrete hydration states within the pocket is independent of pressure (i.e., $\nu(i) - \nu(j)$ is fixed), the pressure dependence of the pocket hydration free energies can be expressed as

$$\Delta G_p(n) = \Delta G_1(n) + (P - 1\ \text{bar}) \times \Delta\nu(n) \tag{4}$$

Here $\Delta G_1(n)$ is the pocket hydration free energy at 1 bar pressure and $\Delta\nu(n)$ is the relative pocket hydration volume. We can subsequently obtain $\Delta G_1(n)$ and $\Delta\nu(n)$ by linear regression of the pocket free energies from simulation obtained following eq 3 as a function of pressure. The occupation probabilities can subsequently be recovered from eq 4 following the relationship

$$p(n) = \alpha \exp\left(-\frac{\Delta G_p(n)}{kT}\right) \tag{5a}$$

where the normalization constant α is determined as

$$\alpha = \frac{1}{\sum_{n=0}^{\infty} \exp\left(-\frac{\Delta G(n)}{kT}\right)} \tag{5b}$$

Taken together, we refer to this as the hydration distribution model (hdist).

The relative hydration free energies of OA for a number of different hydration states (n) are plotted as a function of pressure in Figure 8. The free energies are approximately linear

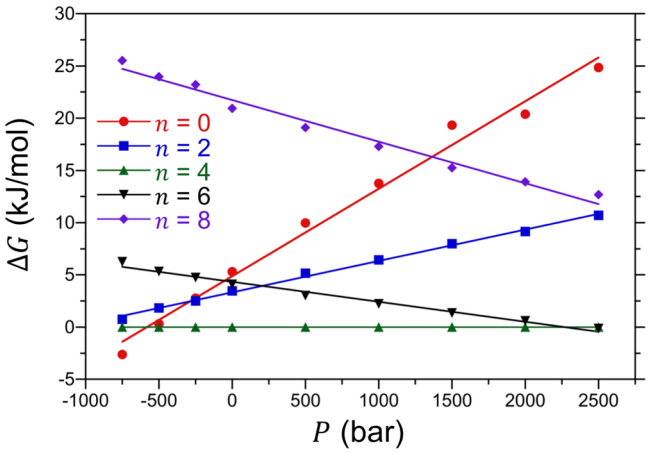

Figure 8. Relative pocket hydration free energies for DEMOA for water occupancy states of n = 0, 2, 4, 6, and 8 evaluated using eq 3 as a function of pressure. Points indicate simulation results, and lines indicate fits to eq 4. The figure symbols are defined in the legend. Error bars are neglected for clarity.

functions pressure, as described by eq 4, consistent with the assumption that the waters in the pocket are to a first approximation incompressible. Qualitatively similar results were obtained for all of the cavitands. In Figures 9 and 10, we plot $\Delta G_1(n)$ and $\Delta\nu(n)$, respectively, for OA obtained from least-squares fitting of the hydration distribution model. As suggested by the hydration state distributions discussed above, $\Delta G_1(n)$ for OA (Figure 9) is approximately parabolic (i.e., Gaussian distribution) near its minimum at $n = 4$. The free energy for the dry state ($n = 0$), however, is significantly lower than would be anticipated based on a quadratic polynomial. The fitted hydration volumes (Figure 10), on the other hand, are a decreasing function of the number of waters within the pocket, consistent with the partial molar volume of the cavitand decreasing as the pocket fills with water. If the volumes of water within the pocket matched that of water in the bulk, then we would expect $\Delta\nu(n)$ to be given as

$$\Delta\nu(n) \approx (4 - n) \times \nu_w \tag{6}$$

where $\nu_w = 18.06\ \text{cm}^3/\text{mol}$ corresponds to the molar volume of bulk water. The bulk water approximation semiquantitatively captures the n of the hydration volume; however, the fitted

https://dx.doi.org/10.1021/acs.jpcb.0c02568
J. Phys. Chem. B XXXX, XXX, XXX−XXX

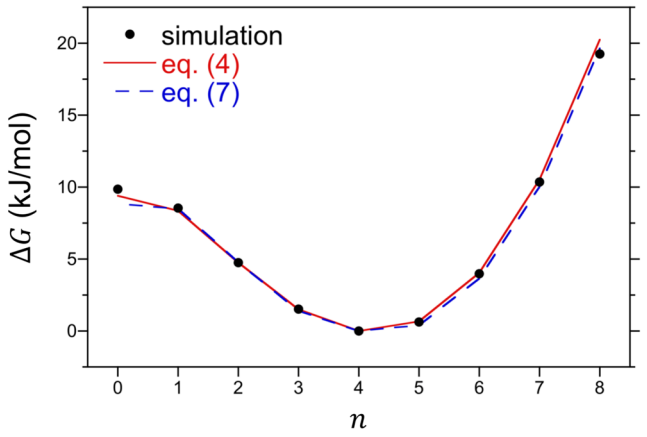

Figure 9. Relative pocket hydration free energies for OA at 25 °C and 1 bar evaluated from simulation (via eq 3) and fits to the hydration distribution (hdist, eq 4) and unified distribution (udist, eq 7) models. The figure symbols are defined in the legend. Simulation error bars are comparable in size or smaller than the symbols.

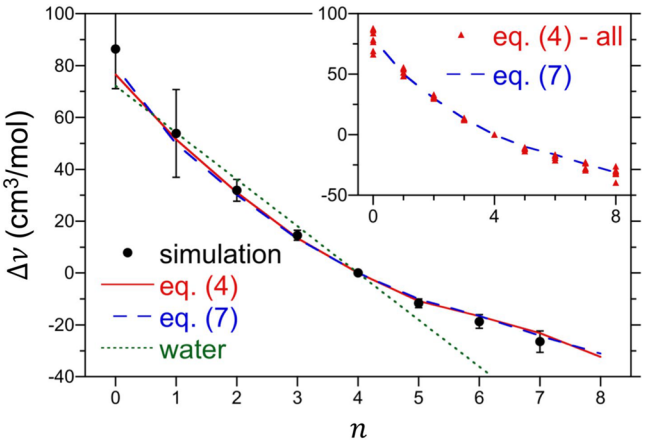

Figure 10. Relative pocket hydration volumes for OA at 25 °C evaluated directly from simulation at 1 bar (eq 1) and fits to the hydration distribution (hdist, eq 4) and unified distribution (udist, eq 7) models. We compare these results against the relative volumes one would obtain using the bulk volume of water following eq 6. The inset figure compares the volumes determined from eq 4 for all of the simulated hosts against those determined from the unified distribution model (eq 7). The figure symbols are defined in the legend. Simulation error bars in the main figure indicate one standard deviation.

values of $\Delta\nu(n)$ deviate from linearity (Figure 10). Specifically, $\Delta\nu(n)$ is concave up, with the volume of the first water that enters the cavity, $\Delta\nu(0) - \Delta\nu(1) = 25.0$ cm^3/mol, considerably greater than that of the bulk, and the volume of the seventh water that enters the cavity, $\Delta\nu(6) - \Delta\nu(7) = 6.6$ cm^3/mol, considerably less than that of the bulk. Thus, water is compressed as we try to squeeze more and more waters into the pocket. We obtain excellent agreement comparing the changes in the relative partial molar volumes of OA as a function of the number of waters in its pocket determined directly from simulation (eq 1) against that for the hydration distribution model, giving us confidence that the model accurately reflects the physical volume of the cavitand. Interestingly, while $\Delta G_1(n)$ is distinct for each of the cavitands, the $\Delta\nu(n)$ values for all of the cavitands are approximately equal to one another (Figure 10, inset).

We compare the mean pocket hydration numbers obtained from the hydration distribution model against those determined from simulation in Figure 7. Overall, the model does an excellent job describing the water adsorption isotherms to the cavitand pockets, validating the assumptions underlying the model. Moreover, the model allows us to evaluate the hydration numbers at pressures not considered in our simulations and more clearly observe the sigmoidal shapes of the binding isotherms.

The differences between the binding isotherms for all of the hosts reported in Figure 7 to a first approximation appear to be horizontally shifted relative to one another. In addition, the relative cavitand volumes obtained from fitting eq 4 to the simulation results are quantitatively similar to one another (Figure 10, inset). We therefore propose that the water adsorption isotherms for all of the hosts can be fitted to a unified adsorption isotherm following the functional form for the free energy

$$\Delta G_p(n) = \Delta G_1^*(n) + (P + P_{shift} - 1\ \text{bar})\Delta\nu^*(n) \qquad (7)$$

where $\Delta G_1^*(n)$ and $\Delta\nu^*(n)$ correspond to the universal pocket hydration free energy and hydration volume and P_{shift} is a host dependent pressure shift measured relative to OA (i.e., P_{shift} = 0 for OA). We refer to this as the unified distribution model (udist). The parameters in eq 7 (i.e., $\Delta G_1^*(n)$, $\Delta\nu^*(n)$, and P_{shift}) have subsequently been obtained by performing a nonlinear least-squares fit to the pocket hydration free energies of all the simulated cavitands.

The unified distribution model is compared against the mean hydration numbers for all of the cavitands in Figure 11

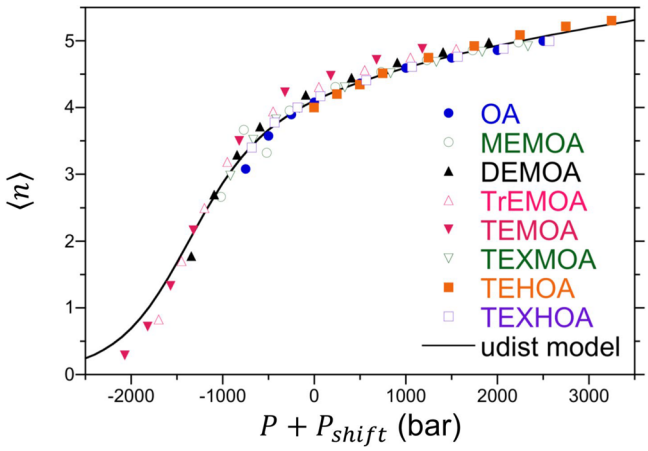

Figure 11. Unified adsorption isotherm for all of the simulated cavitand hosts as a function of effective pocket pressure ($P + P_{shift}$) at 25 °C. Points indicate simulation results, and lines indicate fits to the unified distribution model (eq 7). The figure symbols are defined in the legend. Error bars are comparable in size or smaller than the symbols.

collapsed onto a single adsorption isotherm using the fitted shift pressures. Overall, the unified adsorption isotherm achieves an excellent quantitative description of water adsorption over the entire pressure range. The fitted results for $\Delta G_1^*(n)$, $\Delta\nu^*(n)$, and P_{shift} are reported in Figures 9, 10, and 12, respectively. We observe excellent agreement between the universal results for $\Delta G_1^*(n)$ and $\Delta\nu^*(n)$ with $\Delta G_1(n)$ and $\Delta\nu(n)$ for OA (Figures 9 and 10), establishing OA as an excellent reference host to describe water adsorption. P_{shift}, on

https://dx.doi.org/10.1021/acs.jpcb.0c02568
J. Phys. Chem. B XXXX, XXX, XXX−XXX

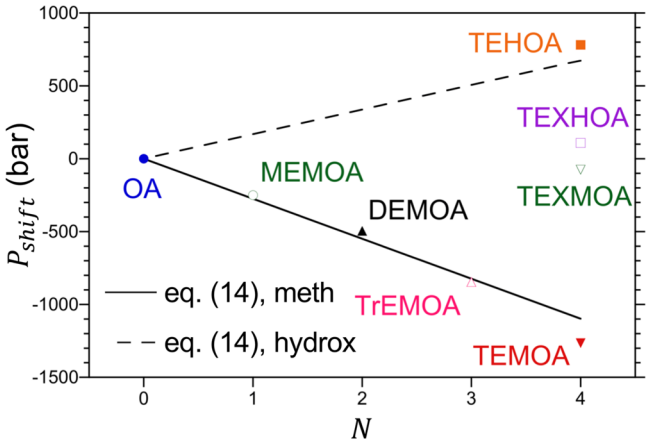

Figure 12. Shift pressures for the unified distribution model (eq 7) and capillary evaporation models for all of the hosts as a function of the number of functional groups *N*. The shift pressures are measured relative to the parent cavitand OA. The points indicate shift pressures for the unified distribution model (eq 7) obtained from fits to all of the simulated hosts. The specific hosts are identified next to the points. The lines indicated shift pressures obtained for the capillary evaporation model (eq 14) for *endo*-methyl and *endo*-hydroxyl functionalization. The capillary evaporation model assumes the shift pressures of the *exo*-functionalized hosts are zero.

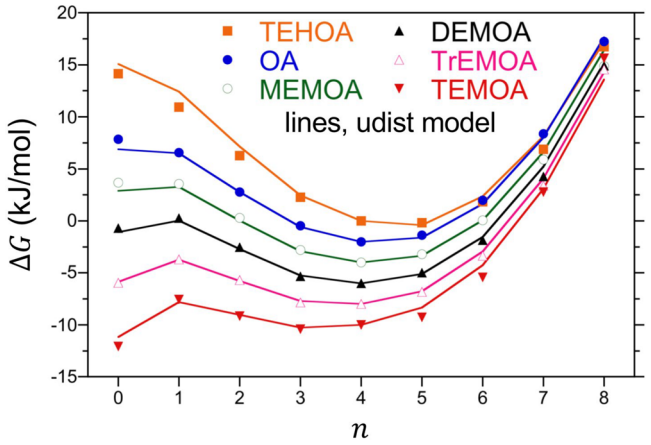

Figure 13. Impact of increasing portal hydrophobicity on relative pocket hydration free energies for the series of *endo*-functionalized hosts TEHOA, OA, MEMOA, DEMOA, TrEMOA, and TEMOA at 25 °C and 1 bar. Points indicate simulation results (eq 3), and lines indicate fits to the unified distribution model (eq 7). The figure symbols are defined in the legend. Simulation error bars are comparable in size or smaller than the symbols. Results are successively shifted downward by 2 kJ/mol from TEHOA to TEMOA for clarity.

the other hand, shows distinct trends with the degree and polarity of the portal functionalization. The largest effect is observed for *endo*-methyl functionalization, with P_{shift} monotonically decreasing from OA to TEMOA with each added methyl group, corresponding to increasing destabilization wetted state by methyl functionalization. In the case of *endo*-hydroxyl functionalization, TEHOA exhibits a positive value for P_{shift}, corresponding to stabilization of the wetted state within the pocket. The magnitude of P_{shift} for TEHOA is only about 60% that for TEMOA, however, indicating that *endo*-methyl functionalization plays a greater role in pocket hydration than *endo*-hydroxyl functionalization. As for the *exo*-methyl groups, TEXMOA exhibits a negative value of P_{shift}, although its magnitude is less than that for MEMOA despite the fact TEXMOA has 4 times as many methyl groups. Similarly, TEXHOA exhibits a positive value for P_{shift} that is lower in magnitude than that for TEHOA. We conclude then that, while *exo*-functionalization plays a role in stabilizing/destabilizing water within pocket, the magnitude of this effect is not as significant as that observed for *endo*-functionalization.

Figure 13 illustrates the pocket hydration free energies of the *endo*-functionalized hosts TEHOA, OA, MEMOA, DEMOA, TrEMOA, and TEMOA in order of increasing hydrophobicity at 1 bar from simulation and fitted to the unified distribution model. Overall, the unified distribution model provides an excellent quantitative description of the pocket hydration free energies for these cavitands, supporting the proposition that the impact of portal functionalization can be treated as a shift in the effective pressure. Importantly, increasing the hydrophobicity of the pocket portal leads to systematic stabilization of the dry state, as indicated by the increasing depth of $\Delta G_1(0)$. Even for TEHOA, however, the free energy exhibits a shoulder at $n = 0$, suggesting a latent inclination for TEHOA's pocket to dry. This inclination subsequently becomes dominant for TEMOA. For the hosts MEMOA through TEMOA, the model predicts the dry state is separated from the wet state by a free energy barrier (i.e., maximum) at $n = 1$. This supports the proposition that the water adsorption within the cavitand pockets is akin to a two-state-like vapor/liquid transition, albeit on a microscopic scale. Presumably, if we could make the pocket more hydrophobic, we would expect to observe only a single free energy minimum for the dry state. The lack of additional *endo* sites and complication of adding conformational degrees of freedom for larger functional groups, however, suggests that this may not be easily achieved.

Capillary Evaporation Model of Cavitand Hydration. Here we describe a capillary evaporation model in an effort to rationalize the impact of portal functionalization on water adsorption into cavitand pockets. This model is based on the idea that the system thermodynamics can be described using interfacial free energies associated with the cavitand surfaces contacting water or a vacuum (water absence), which is clearly an approximation when applied to the molecular level. Nevertheless, this model reproduces many of the salient elements of water adsorption described above. Our physical picture of the cavitand in water underlying our capillary evaporation model is illustrated in Figure 14. Here, the parent cavitand, OA, is assumed to be a bowl-shaped pocket (indicated in gray) with an inner surface area of A_{pock}. The portal to the binding pocket (indicated in green) has a cross-sectional area of A_{port} in the absence of any added *endo*-functional groups (methyl or hydroxyl). Finally, each *endo*-functional group (indicated in red) ringing the pocket blocks an area of A_{func} from the portal. The volume of the cavitand, ν_{cav}, is defined by the region bounded by the pocket and portal. We neglect the impact of *exo*-functional groups in this model, which were shown above to have a minimal impact on water adsorption relative to OA.

The cavitand pocket is open to bulk water, permitting free exchange through the portal. In this case, water adsorption equilibrium is described by the grand potential of the open system associated with the cavitand volume.[7,8,42,43] The grand potential of the dry pocket with *N* *endo*-functional groups is

$$\Omega_{dry} = \gamma_{cv}A_{pock} + \gamma_{lv}(A_{port} - NA_{func}) + \gamma_{fv}NA_{func} \quad (8)$$

https://dx.doi.org/10.1021/acs.jpcb.0c02568
J. Phys. Chem. B XXXX, XXX, XXX−XXX

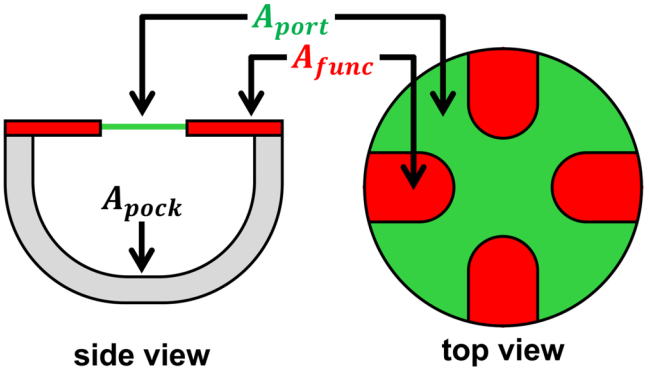

Figure 14. Schematic illustration of the *endo*-functionalized hosts used to develop the capillary evaporation model. The host pocket, portal, and functional groups are identified in gray, green, and red, respectively, along with their corresponding areas, A_{pock}, A_{port}, and A_{func}. The cavitand volume, ν_{cav}, is bounded by the pocket and portal surfaces.

where γ_{cv}, γ_{lv}, and γ_{fv} are the cavitand/vacuum, liquid water/vacuum, and functional group/vacuum interfacial free energies and N (= 0−4) is the number of *endo* functional groups. The dry state here is assumed to be a vacuum rather than a vapor, as would normally be assumed for larger volumes. The pressure inside the dry pocket is zero (i.e., vacuum) and therefore does not contribute to eq 8. The grand potential of the wet pocket is

$$\Omega_{wet} = \gamma_{cl}A_{pock} + \gamma_{fl}NA_{func} - P\nu_{cav} \tag{9}$$

where γ_{cl} and γ_{fl} are the cavitand/liquid water and functional group/liquid water interfacial free energies, respectively, and P is the bulk pressure.

Given that the probability of observing the dry or wet state is proportional to the Boltzmann weighting of their respective grand potentials (i.e., $p_{dry/wet} \propto \exp(-\Omega_{dry/wet}/kT)$), the probability of observing the wet state is

$$p_{wet} = \frac{\exp(-\Omega_{wet}/kT)}{\exp(-\Omega_{wet}/kT) + \exp(-\Omega_{dry}/kT)} = \frac{1}{1 + \exp(\Delta\Omega/kT)} \tag{10}$$

where

$$\Delta\Omega = \Omega_{wet} - \Omega_{dry} = (\gamma_{fl} + \gamma_{lv} - \gamma_{fv})NA_{func} + [(\gamma_{cl} - \gamma_{cv})A_{pock} - \gamma_{lv}A_{port}] - P\nu_{cav} \tag{11}$$

Thus, based on this model, water is expected to follow a Fermi function (eq 10), characteristic of two-state-like thermodynamic equilibrium. Considering that ν_{cav} is positive, eq 10 predicts the cavitand is dry for low pressures (i.e., $p_{wet} = 0$ for low or even negative P) and wetting occurs with increasing pressure (i.e., $p_{wet} = 1$ for large P). This agrees with our simplest expectations from above. The transition point between dry and wet states ($\Delta\Omega = 0$) occurs at the pressure

$$P_{trans} = \frac{(\gamma_{fl} + \gamma_{lv} - \gamma_{fv})NA_{func} + [(\gamma_{cl} - \gamma_{cv})A_{pock} - \gamma_{cl}A_{port}]}{\nu_{cav}} \tag{12}$$

which may occur at positive or negative pressures depending on the degree of rim functionalization, and values of the associated interfacial free energies.

Assuming that ν_{cav} is the same across all of the hosts examined, the capillary evaporation model provides a direct rationalization of the collapse of the water adsorption isotherms onto a universal curve and the shift pressures. Assuming OA (N = 0) as a reference host, the shift pressure can be determined by equating eq 11 for a functionalized host with that of OA at a pressure of $P + P_{shift}$

$$(\gamma_{fl} + \gamma_{lv} - \gamma_{fv})NA_{func} + [(\gamma_{cl} - \gamma_{cv})A_{pock} - \gamma_{cl}A_{port}] - P\nu_{cav} = [(\gamma_{cl} - \gamma_{cv})A_{pock} - \gamma_{cl}A_{port}] - (P + P_{shift})\nu_{cav} \tag{13}$$

which yields

$$P_{shift} = -\frac{(\gamma_{fl} + \gamma_{lv} - \gamma_{fv})A_{func}}{\nu_{cav}}N \tag{14}$$

Based on this model, we expect the shift pressure to be a linear function of the degree of *endo*-functionalization, qualitatively similar to that reported for the sequence OA to TEMOA in Figure 12. The negative shift pressures observed for methyl functionalization can be explained within the context of eq 14. Specifically, we expect for liquid water that γ_{fl} is positive, that water unfavorably wets hydrophobic functional groups, and that γ_{lv} is greater than γ_{fv} given the lower surface tension of water compared to that of liquid alkanes. As a result, P_{shift} is anticipated to be negative for methyl group functionalization, as observed in Figure 12. For the hydroxyl groups to exhibit a positive shift pressure, we must have the combination of terms $\gamma_{fv} - \gamma_{fl}$ to be greater than γ_{fl}. This could result from a combination of wetting of the hydroxyl group by water to be very favorable ($\gamma_{fl} < 0$) and exposure of the group to a vacuum being exceptionally unfavorable ($\gamma_{fv} > \gamma_{lv}$). A definitive rationalization for the positive shift pressures of the hydroxy groups, however, is not immediately apparent based on macroscopic considerations.

A shortcoming of applying the capillary evaporation model as described above is that eq 10 only describes the probability of observing a dry or wet state, while the adsorption isotherms reported above indicate continued filling of the cavitand with increasing pressure above the wetting transition. This suggests the overall compressibility of the water within the pocket should be taken into account. We subsequently model the mean wet state pocket water occupancy as

$$n_{wet} = n_0 \exp[\kappa_0(P + P_{shift})] \tag{15}$$

where n_0 is the mean wet state occupancy at zero pressure and κ_0 is the compressibility of water within the host pocket. While we assumed zero compressibility of the individual water occupancy states in eqs 4 and 7 above, the hydration distribution models described above do capture the compression of waters within the pocket (e.g., Figure 7). This is a result of the fact that equilibrium tips toward states with lower volumes in response to increasing pressure (e.g., Figure 10), compressing waters within the pocket as described by eq 15.

https://dx.doi.org/10.1021/acs.jpcb.0c02568
J. Phys. Chem. B XXXX, XXX, XXX−XXX

The effective pressure of water inside the wetted pocket in this expression is taken as $P + P_{shift}$. This is necessary for the model to achieve a universal collapse. In this case, the shift pressure can be interpreted as being analogous to a Laplace pressure, the pressure differential across a curved interface.

Given that the application of macroscopic interfacial free energies down to molecular-scale phenomena is debatable and that the individual interfacial free energies are not independent of one another in eq 11, we combine them together as

$$\alpha = (\gamma_{fl} + \gamma_{lv} - \gamma_{fv})A_{func} \tag{16a}$$

and

$$\beta = (\gamma_{cl} - \gamma_{cv})A_{pock} - \gamma_{cl}A_{port} \tag{16b}$$

The mean pocket occupancy for the capillary evaporation model is finally determined as

$$\langle n \rangle = p_{wet} n_{wet} + (1 - p_{wet}) n_{dry} = p_{wet} n_{wet} = \frac{n_0 \exp[\kappa_0 (P + P_{shift})]}{1 + \exp\{\beta - (P + P_{shift})\nu_{cav}/kT\}} \tag{17}$$

where the mean dry state occupancy, n_{dry}, is zero. The shift pressure in here is determined as $P_{shift} = -\alpha N/\nu_{cav}$, where α adopts different values for methyl and hydroxyl functional groups. In this expression, α, β, n_0, κ_0, and ν_{cav} are treated as fitting parameters. To connect the volume of the cavitand pocket to the molecular scale packing of water within its confines, we assume

$$\nu_{cav} = n_0/\rho_w \tag{18}$$

where ρ_w here is the bulk number density of water ($1/\rho_w$ = 30 Å^3) at atmospheric pressure.

In Figure 15, we compare the least-squares fit of the capillary evaporation model (fit parameters reported in Table 1) as a function of $P + P_{shift}$ against the simulation results for water adsorption in the *endo*-functionalized hosts: OA, MEMOA, DEMOA, TrEMOA, TEMOA, and TEHOA. Overall, the model provides a near quantitative description of water adsorption as a function of pressure, supporting the assumption that water adsorption within hosts is well described as a two-state equilibrium. Moreover, we find semiquantitative agreement between P_{shift}'s obtained from the capillary evaporation model and those obtained by fitting eq 7 (Figure 12). Consideration of specific parameters reported in Table 1 further supports the reasonableness of the proposed capillary evaporation model. Given the fact that water loses hydrogen-bonding partners when it enters the host pocket, it is sensible to expect adsorbed waters to be more compressible. This is borne out comparing the fitted compressibility of water in the pocket against that for bulk TIP4P/Ew water, 4.75 × 10^{-5} bar^{-1}; that is, the fitted compressibility is 50% greater than the bulk compressibility. For a wetted OA pocket at atmospheric pressure with n_0 = 4.269 waters, the universal binding model described in the previous section anticipates a pocket volume (e.g., Figure 10) of $\Delta\Delta\nu^*(0, n_0) = \Delta\nu^*(0) - \Delta\nu^*(4.269)$ = 82.2 cm^3/mol = 136 Å^3 ($\Delta\nu^*(4.269)$ was determined by interpolation between $\Delta\nu^*(4)$ and $\Delta\nu^*(5)$). This volume is in good agreement with that obtained by fitting ν_{cav}, differing only by ∼7%. It may be thought, however, that the assumption that the cavitand volume is described by eq 18 is erroneous. If we relax this assumption and make ν_{cav} itself a fitting parameter, we obtain a best fit value of 128.9 Å^3 = 77.6 cm^3/mol, differing by less than 1%. Taken together, these observations support our proposition that drying of supramolecular host pockets is driven by capillary evaporation.

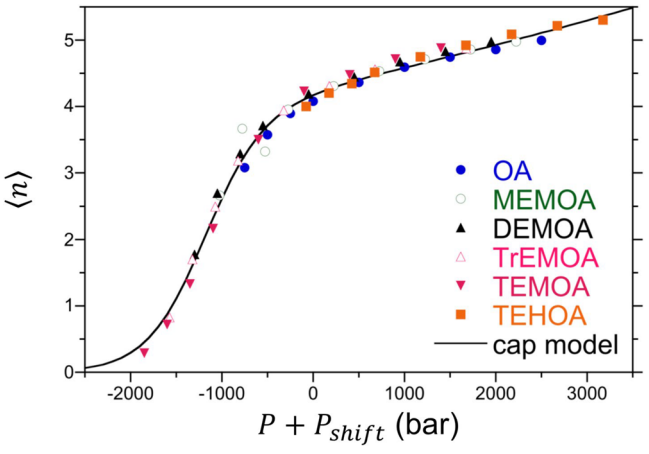

Figure 15. Comparison between the mean pocket hydration numbers as a function of the effective pocket pressure ($P + P_{shift}$) for the *endo*-functionalized hosts determined from simulation and the capillary evaporation model (eq 17) at 25 °C. The figure symbols are defined in the legend. Error bars are comparable in size or smaller than the symbols.

Table 1. Capillary Evaporation Model Parameters Obtained by Least-Squares Fitting of Simulation Results for OA, MEMOA, DEMOA, TrEMOA, TEMOA, and TEHOA

parameter	value
n_0	4.269
κ_0	7.185 × 10^{-5} bar^{-1}
$\nu_{cav} = n_0/\rho_w$	128.1 Å^3
$-\alpha_{meth}/\nu_{cav}$	−274.4 bar
$-\alpha_{hydrox}/\nu_{cav}$	168.2 bar
β	−9.341 kJ/mol

CONCLUSIONS

In conclusion, we have reported a molecular simulation and theoretical analysis of the adsorption of water into the hydrophobic pockets of deep-cavity cavitands in water over a broad range of pressures. The portals of these cavitands were functionalized with hydrophobic (methyl) and hydrophilic (hydroxyl) groups, that adopted either inward (*endo*) or upward (*exo*) orientations with respect to the pocket. Our simulations found that wetting of the pocket, as captured by the mean water occupancy, is directly controlled by hydrophobicity of the portal, with more hydrophobic groups tilting the equilibrium toward lower pocket occupancies and hydrophilic groups tilting toward higher pocket occupancies. Directing the functional groups in an *exo* (upward) orientation from the pocket significantly reduces their impact on pocket occupancy, indicating the effect on pocket hydration is local.

From a thermodynamic perspective, water adsorption within host pockets appears to be governed by equilibrium between dry (empty) and wet (filled) states, separated by a free energy barrier associated with the first water entering the host pocket. Filling of the pocket is driven by lowering of the host volume with increasing pressure, in accordance with Le Chatelier's principle. Considering the pocket occupancy distributions, our analysis demonstrated that water adsorption across all hosts

https://dx.doi.org/10.1021/acs.jpcb.0c02568
J. Phys. Chem. B XXXX, XXX, XXX−XXX

could be collapsed onto a unified adsorption isotherm, in which the adsorption isotherms of chemically distinct cavitands could be mapped onto one another via a shift pressure. The shift pressure is positive for hydrophilic functional groups and progressively negative for hydrophobic functional groups.

Finally, we demonstrated that the adsorption equilibrium could be described by a two-state capillary evaporation model, which describes equilibrium as resulting from a balance of interfacial free energies for wetting/drying of the internal surfaces of the cavitand and the bulk system pressure. This model captures many of the salient features observed from our simulations, including the collapse of the adsorption isotherms for a range of cavitands onto a unified isotherm and the signs of the shift pressures for the hydrophobic and hydrophilic functional groups. We note, however, that it is surprising that the hydration of our cavitands can be modeled following a two-state model, describing equilibrium between two distinct thermodynamic states, while our simulations find a wide range of pocket hydration state numbers that may be observed. Nevertheless, the hydration probability distributions obtained from simulation (e.g., Figures 4a and 6) suggest two states with fluctuations about the means of the two states. In the case of the relatively small volumes of the cavitand pockets, those fluctuations are comparatively large, lowering the barrier between states. In the case of significantly larger observation volumes, like that between hydrophobic plates,[6−8,10,44] the barrier is more significant with fluctuations playing a smaller role so that the two states are more clear. As a result, we expect the parameters of the proposed two-state evaporation model to not necessarily scale to macroscopic confinements.

This work demonstrates that the wetting behavior of a supramolecular host pocket can be directly tuned by functionalizing the portal to the binding site. In particular, the pocket can be dewetted using hydrophobic functional groups or more strongly wetted using hydrophilic functional groups. This, in turn, is sure to impact the binding of guests by the host, since evacuation of the pocket is a necessary step for the guest to settle into the binding site.

AUTHOR INFORMATION

Corresponding Author

Henry S. Ashbaugh − *Department of Chemical and Biomolecular Engineering, Tulane University, New Orleans, Louisiana 70118, United States;* orcid.org/0000-0001-9869-1900; Email: hanka@tulane.edu

Authors

Du Tang − *Department of Chemical and Biomolecular Engineering, Tulane University, New Orleans, Louisiana 70118, United States*

Tobias Dwyer − *Department of Chemical Engineering, University of Arkansas, Fayetteville, Alaska 72701, United States*

Hussain Bukannan − *Department of Chemical and Biomolecular Engineering, Tulane University, New Orleans, Louisiana 70118, United States*

Odella Blackmon − *Department of Chemistry, William Carey University, Hattiesburg, Mississippi 39401, United States*

Courtney Delpo − *Department of Chemistry, Ursinus College, Collegeville, Pennsylvania 19426, United States*

J. Wesley Barnett − *Department of Chemical and Biomolecular Engineering, Tulane University, New Orleans, Louisiana 70118, United States*

Bruce C. Gibb − *Department of Chemistry, Tulane University, New Orleans, Louisiana 70118, United States;* orcid.org/0000-0002-4478-4084

Complete contact information is available at: https://pubs.acs.org/10.1021/acs.jpcb.0c02568

Notes

The authors declare no competing financial interest.

ACKNOWLEDGMENTS

We gratefully acknowledge financial support from the NSF-DMR (No. 1460637), NSF-CBET (Nos. 1403167 and 1805167), and the Center for Engaged Learning and Teaching at Tulane University (H.B.). We also thank the Louisiana Optical Network Initiative (www.loni.org) for computational support.

REFERENCES

(1) Stillinger, F. H. Structure in aqueous solutions of nonpolar solutes from the standpoint of scaled-particle theory. *J. Solution Chem.* **1973**, *2*, 141−158.

(2) Lum, K.; Chandler, D.; Weeks, J. D. Hydrophobicity at small and large length scales. *J. Phys. Chem. B* **1999**, *103* (22), 4570−4577.

(3) Weeks, J. D.; Katsov, K.; Vollmayr, K. Roles of repulsive and attractive forces in determining the structure of nonuniform liquids: Generalized mean field theory. *Phys. Rev. Lett.* **1998**, *81* (20), 4400−4403.

(4) Hummer, G.; Garde, S. Cavity expulsion and weak dewetting of hydrophobic solutes in water. *Phys. Rev. Lett.* **1998**, *80* (19), 4193−4196.

(5) Ashbaugh, H. S.; Pratt, L. R. Colloquium: Scaled particle theory and the length scales of hydrophobicity. *Rev. Mod. Phys.* **2006**, *78* (1), 159−178.

(6) Chandler, D. Interfaces and the driving force of hydrophobic assembly. *Nature* **2005**, *437* (7059), 640−647.

(7) Cerdeirina, C. A.; Debenedetti, P. G.; Rossky, P. J.; Giovambattista, N. Evaporation length scales of confined water and some common organic liquids. *J. Phys. Chem. Lett.* **2011**, *2* (9), 1000−1003.

(8) Ashbaugh, H. S. Solvent cavitation under solvophobic confinement. *J. Chem. Phys.* **2013**, *139*, No. 064702.

(9) Altabet, Y. E.; Haji-Akbari, A.; Debenedetti, P. G. Effect of material flexibility on the thermodynamics and kinetics of hydrophobically induced evaporation of water. *Proc. Natl. Acad. Sci. U. S. A.* **2017**, *114* (13), E2548−E2555.

(10) Remsing, R. C.; Xi, E.; Vembanur, S.; Sharma, S.; Debenedetti, P. G.; Garde, S.; Patel, A. J. Pathways to dewetting in hydrophobic confinement. *Proc. Natl. Acad. Sci. U. S. A.* **2015**, *112* (27), 8181−8186.

(11) Truskett, T. M.; Debenedetti, P. G.; Torquato, S. Thermodynamic implications of confinement for a waterlike fluid. *J. Chem. Phys.* **2001**, *114* (5), 2401−2418.

(12) Huang, D. M.; Chandler, D. The hydrophobic effect and the influence of solute-solvent attractions. *J. Phys. Chem. B* **2002**, *106* (8), 2047−2053.

(13) Patel, A. J.; Varilly, P.; Jamadagni, S. N.; Hagan, M. F.; Chandler, D.; Garde, S. Sitting at the Edge: How Biomolecules use Hydrophobicity to Tune Their Interactions and Function. *J. Phys. Chem. B* **2012**, *116* (8), 2498−2503.

(14) Godawat, R.; Jamadagni, S. N.; Garde, S. Characterizing hydrophobicity of interfaces by using cavity formation, solute binding, and water correlations. *Proc. Natl. Acad. Sci. U. S. A.* **2009**, *106* (36), 15119−15124.

(15) Collins, M. D.; Hummer, G.; Quillin, M. L.; Matthews, B. W.; Gruner, S. M. Cooperative water filling of a nonpolar protein cavity observed by high-pressure crystallography and simulation. *Proc. Natl. Acad. Sci. U. S. A.* **2005**, *102* (46), 16668−16671.

(16) Zhu, F. Q.; Hummer, G. Pore opening and closing of a pentameric ligand-gated ion channel. *Proc. Natl. Acad. Sci. U. S. A.* **2010**, *107* (46), 19814−19819.
(17) Beckstein, O.; Sansom, M. S. P. A hydrophobic gate in an ion channel: the closed state of the nicotinic acetylcholine receptor. *Phys. Biol.* **2006**, *3* (2), 147−159.
(18) Anishkin, A.; Sukharev, S. Water dynamics and dewetting transitions in the small mechanosensitive channel MscS. *Biophys. J.* **2004**, *86* (5), 2883−2895.
(19) Qvist, J.; Davidovic, M.; Hamelberg, D.; Halle, B. A dry ligand-binding cavity in a solvated protein. *Proc. Natl. Acad. Sci. U. S. A.* **2008**, *105* (17), 6296−6301.
(20) Setny, P.; Wang, Z.; Cheng, L. T.; Li, B.; McCammon, J. A.; Dzubiella, J. Dewetting-Controlled Binding of Ligands to Hydrophobic Pockets. *Phys. Rev. Lett.* **2009**, *103* (18), 187801.
(21) Setny, P.; Baron, R.; McCammon, J. A. How Can Hydrophobic Association Be Enthalpy Driven? *J. Chem. Theory Comput.* **2010**, *6* (9), 2866−2871.
(22) Baron, R.; Setny, P.; McCammon, J. A. Water in Cavity-Ligand Recognition. *J. Am. Chem. Soc.* **2010**, *132* (34), 12091−12097.
(23) Hummer, G. Molecular binding: Under water's influence. *Nat. Chem.* **2010**, *2* (11), 906−907.
(24) Snyder, P. W.; Mecinovic, J.; Moustakas, D. T.; Thomas, S. W.; Harder, M.; Mack, E. T.; Lockett, M. R.; Heroux, A.; Sherman, W.; Whitesides, G. M. Mechanism of the hydrophobic effect in the biomolecular recognition of arylsulfonamides by carbonic anhydrase. *Proc. Natl. Acad. Sci. U. S. A.* **2011**, *108* (44), 17889−17894.
(25) Smithrud, D. B.; Wyman, T. B.; Diederich, F. Enthalpically driven cyclophane-arene inclusion complexation: solvent-dependent calorimetric studies. *J. Am. Chem. Soc.* **1991**, *113* (14), 5420−5426.
(26) Biedermann, F.; Nau, W. M.; Schneider, H. J. The hydrophobic effect revisited-studies with supramolecular complexes imply high-energy water as a noncovalent driving force. *Angew. Chem., Int. Ed.* **2014**, *53* (42), 11158−11171.
(27) Biedermann, F.; Vendruscolo, M.; Scherman, O. A.; De Simone, A.; Nau, W. M. Cucurbit 8 uril and Blue-Box: High-energy water release overwhelms electrostatic interactions. *J. Am. Chem. Soc.* **2013**, *135* (39), 14879−14888.
(28) Gibb, C. L. D.; Gibb, B. C. Well-defined, organic nanoenvironments in water: The hydrophobic effect drives a capsular assembly. *J. Am. Chem. Soc.* **2004**, *126* (37), 11408−11409.
(29) Jordan, J. H.; Gibb, B. C. Molecular containers assembled through the hydrophobic effect. *Chem. Soc. Rev.* **2015**, *44* (2), 547−585.
(30) Ewell, J.; Gibb, B. C.; Rick, S. W. Water inside a hydrophobic cavitand molecule. *J. Phys. Chem. B* **2008**, *112* (33), 10272−10279.
(31) Barnett, J. W.; Sullivan, M. R.; Long, J. A.; Tang, D.; Nguyen, T.; Ben-Amotz, D.; Gibb, B. C.; Ashbaugh, H. S. Spontaneous drying of non-polar deep-cavity cavitand pockets in aqueous solution. *Nat. Chem.* **2020**, DOI: 10.1038/s41557-020-0458-8.
(32) Abraham, M. J.; Murtola, T.; Schulz, R.; Páll, S.; Smith, J. C.; Hess, B.; Lindahl, E. GROMACS: High performance molecular simulations through multi-level parallelism from laptops to supercomputers. *SoftwareX* **2015**, *1−2*, 19−25.
(33) Nosé, S. A unified formulation of the constant temperature molecular-dynamics methods. *J. Chem. Phys.* **1984**, *81*, 511−519.
(34) Hoover, W. G. Canonical dynamics: Equilibrium phase-space distributions. *Phys. Rev. A: At., Mol., Opt. Phys.* **1985**, *31*, 1695−1697.
(35) Horn, H. W.; Swope, W. C.; Pitera, J. W.; Madura, J. D.; Dick, T. J.; Hura, G. L.; Head-Gordon, T. Development of an improved four-site water model for biomolecular simulations: TIP4P-Ew. *J. Chem. Phys.* **2004**, *120* (20), 9665−9678.
(36) Wang, J. M.; Wolf, R. M.; Caldwell, J. W.; Kollman, P. A.; Case, D. A. Development and testing of a general amber force field. *J. Comput. Chem.* **2004**, *25* (9), 1157−1174.
(37) Jakalian, A.; Bush, B. L.; Jack, D. B.; Bayly, C. I. Fast, efficient generation of high-quality atomic charges. AM1-BCC model: I. Method. *J. Comput. Chem.* **2000**, *21* (2), 132−146.
(38) Frenkel, D.; Smit, B. *Understanding molecular simulation: From algorithms to applications*, 2nd ed.; Academic Press: San Diego, CA, 2001.
(39) Darden, T.; York, D.; Pedersen, L. Particle mesh Ewald - An N.log(N) method for Ewald Sums in large systems. *J. Chem. Phys.* **1993**, *98* (12), 10089−10092.
(40) Hess, B.; Bekker, H.; Berendsen, H. J. C.; Fraaije, J. LINCS: A linear constraint solver for molecular simulations. *J. Comput. Chem.* **1997**, *18* (12), 1463−1472.
(41) Miyamoto, S.; Kollman, P. A. SETTLE - An analytical version of the shake and rattle algorithm for rigid water models. *J. Comput. Chem.* **1992**, *13* (8), 952−962.
(42) Evans, R. Fluids adsorbed in narrow pores: Phase-equlibria and structure. *J. Phys.: Condens. Matter* **1990**, *2* (46), 8989−9007.
(43) Huang, X.; Margulis, C. J.; Berne, B. J. Dewetting-induced collapse of hydrophobic particles. *Proc. Natl. Acad. Sci. U. S. A.* **2003**, *100* (21), 11953−11958.
(44) Giovambattista, N.; Rossky, P. J.; Debenedetti, P. G. Computational Studies of Pressure, Temperature, and Surface Effects on the Structure and Thermodynamics of Confined Water. In *Annual Review of Physical Chemistry*; Johnson, M. A., Martinez, T. J., Eds.; Annual Reviews: Palo Alto, CA, 2012; Vol. *63*, pp 179−200.

https://dx.doi.org/10.1021/acs.jpcb.0c02568
J. Phys. Chem. B XXXX, XXX, XXX−XXX